Doherty-Like Load-Modulated Balanced Amplifier With Decade Bandwidth Enabled by Novel Broadband All-Port-Matched Balun

Pingzhu Gong, *Student Member, IEEE*, Niteesh Bharadwaj Vangipurapu, *Graduate Student Member, IEEE*, Jiachen Guo, *Member, IEEE*, and Kenle Chen, *Senior Member, IEEE*

***Abstract*—This article presents the first demonstration of a decade-bandwidth Doherty-like load-modulated balanced amplifier (DL-LMBA). While a frequency-agnostic, signal-flow-based broadband LMBA theory is recently developed and successfully applied to pseudo-Doherty LMBA (PD-LMBA) to validate its wideband performance both theoretically and experimentally, the broadband potential of DL-LMBA has not yet been thoroughly proven. Leveraging this newly developed theory, this work proves, for the first time, that the ideal broadband load modulation behavior in DL-LMBA can be achieved only when a constant 180° phase offset is maintained between the BA and CA signal paths across the band. This condition fundamentally differs from that of PD-LMBA. The proposed theory enables us to overcome the longstanding bandwidth limitations in DL-LMBA design. Furthermore, based on the signal-flow approach, a novel reflective-type-phase-shifter-based balun (RPB) is proposed to enable the wideband operation of DL-LMBA. To validate the proposed concept, an ultrawideband RF-input DL-LMBA prototype is implemented in GaN technology, covering a frequency range from 0.2 to 2 GHz. Experimental results demonstrate peak output power efficiency ranging from 44% to 67%, and 6-dB output back-off (OBO) efficiency ranging from 43% to 75%.**

***Index Terms*—Balanced amplifier (BA), balun, Doherty, high efficiency, hybrid coupler, load modulation, power amplifier (PA), power divider, quadrature coupler, reflective phase shifter, signal-flow graph, wideband, Wilkinson.**

I. Introduction

As WIRELESS communication systems continue to evolve, the demand for transmitting high-data-rate signals is steadily increasing. To meet this demand, advanced modulation schemes (e.g., OFDM) are employed to enhance spectral efficiency. However, these sophisticated modulation techniques produce signals with large amplitude variations, characterized by a high peak-to-average power ratio (PAPR). When such signals are amplified, power amplifiers (PAs) experience significant efficiency degradation. Furthermore, with the growing number of users and applications of communication devices, a multitude of frequency bands has become available. This expanded spectrum requires PAs to maintain high performance over an increasingly wide frequency range.

To transmit high-PAPR signals efficiently, several techniques have merged for PAs. These include envelope tracking (ET) techniques [1] and various load modulation-based architectures. Examples of the latter include outphasing PAs [2], [3], [4], [5], Doherty PAs (DPAs) [6], [7], [8], [9], [10], [11], [12], [13], [14], [15], [16], [17], [18], and load-modulated balanced amplifiers (LMBAs) [19], [20], [21], [22], [23], [24], [25], [26], [27], [28], [29], [30], [31], [32], [33], [34], [35], [36], [37], [38], [39], [40], [41], [42]. In addition, novel load-modulated PA topologies have been introduced using alternative power combining techniques, such as the circulator load-modulated amplifier (CLMA) [43], the switchless class-G (SLCG) PA [44], [45], [46], and the coupler-Balun load-modulated PA (CBMA) [47]. These advanced PA architectures offer high efficiency across various power levels, enhancing average efficiency when transmitting signals with high PAPR. LMBA, initially proposed in [19], has demonstrated the capability to maintain high efficiency at average power levels across a broad bandwidth. By injecting an additional signal into the isolation port of the output quadrature coupler of the balanced amplifier (BA) via a control amplifier (CA), the load impedance seen by the BA is modulated to lower values as output power increases, thereby enhancing average efficiency.

LMBA can generally operate in one of two modes, defined by the biasing configurations of the BA and CA. In the original configuration, referred to as the Doherty-like LMBA (DL-LMBA) [22], the CA is biased in Class C to function as the peaking amplifier, while the BA operates in Class B or AB as the carrier amplifier. A more recently introduced mode, known as the pseudo-Doherty LMBA (PD-LMBA) [24] or sequential LMBA (SLMBA) [25], reverses these roles: the CA is biased in Class B or AB as the carrier, and the BA is biased in Class C to serve as the peaking amplifier. Notably, PD-LMBA has demonstrated a 10-dB output back-off (OBO) range and ultrawide bandwidth up to a decade (10:1) [48]. Compared to DL-LMBA, PD-LMBA offers a deeper OBO range due to the BA's dual-transistor configuration, which naturally provides greater power-handling capability. However, PD-LMBA also introduces challenges: since the CA operates in saturation even at back-off levels, it suffers from over-driving issues, potentially compromising linearity

Received 22 May 2025; revised 9 July 2025; accepted 20 July 2025. This work was supported in part by the National Science Foundation under Award 1914875 and Award 2218808. *(Corresponding author: Pingzhu Gong.)*

The authors are with the Department of Electrical and Computer Engineering, University of Central Florida, Orlando, FL 32816 USA (e-mail: pingzhu.gong@ucf.edu; kenle.chen@ucf.edu).

Digital Object Identifier 10.1109/TMTT.2025.3592130

and long-term reliability. Furthermore, in technologies where the transistor's optimum load impedance is relatively low [49], [50], the DL-LMBA architecture is preferred due to its low-impedance nature at peak power. In contrast, the PD-LMBA presents a higher peak-power impedance, which may deviate more significantly from the device's optimum load, potentially degrading performance.

For S-matrix-based problems, signal-flow graphs are commonly used as a visual and intuitive analysis tool. While most existing applications of signal-flow graphs focus on power-independent networks, Gong et al. [48] introduce, for the first time, a signal-flow-based approach to model the broadband active load modulation behavior of PD-LMBA. This methodology enables a systematic solution of the phase-alignment problem and provides a fundamental explanation for the inherently wideband performance of PD-LMBA.

While experimental results have shown that single-input PD-LMBA can achieve nearly unlimited bandwidth, single-input DL-LMBA designs in the current literature [22] and [30] are not able to extend the bandwidth beyond one octave. Leveraging the signal-flow-based broadband LMBA theory [48], this work proves, for the first time, that the ideal broadband load modulation behavior in DL-LMBA can be achieved only when a constant 180° phase offset is maintained between the BA and CA signal paths across the band, a condition fundamentally different from that of PD-LMBA. To achieve this constant 180° phase offset over an ultrabroad bandwidth, this article proposes a novel reflective-type-phase-shifter-based balun (RPB) at the input to provide the desired phase offset for BA and CA. This approach enables the DL-LMBA prototype to reach a decade bandwidth, significantly outperforming the state-of-the-art. Compared to our previous conference version [51], this journal article includes a more comprehensive theoretical analysis and additional simulation results of DL-LMBA and the proposed power divider. Furthermore, enhanced modulated signal measurements with digital predistortion (DPD) are presented, demonstrating improved linearity and linearizability compared to our decade-bandwidth PD-LMBA prototype [48].

II. Ultrawideband DL-LMBA Theory Based on Signal-Flow Graph

In the previously reported LMBA theory [19], [24], the load modulation behavior is analyzed using Z-matrix, which is valid only at a single frequency. As a result, this theory does not provide a rigorous explanation of the broadband performance of LMBA. Moreover, the impact of matching networks (MNs), which play a critical role in the phase-alignment problem, is not considered in the original analysis. To overcome these challenges, we propose a signal-flow-based broadband LMBA theory in our previous work [48], which accounts for the frequency-dependent behavior of quadrature couplers and other circuit components through an S-matrix-based signal-flow graph. In [48], a frequency-dependent S-matrix is introduced to accurately model the broadband characteristics of an ideal quadrature coupler. Based on this theoretical framework, a decade-bandwidth PD-LMBA is developed and experimentally validated, demonstrating superior broadband performance.

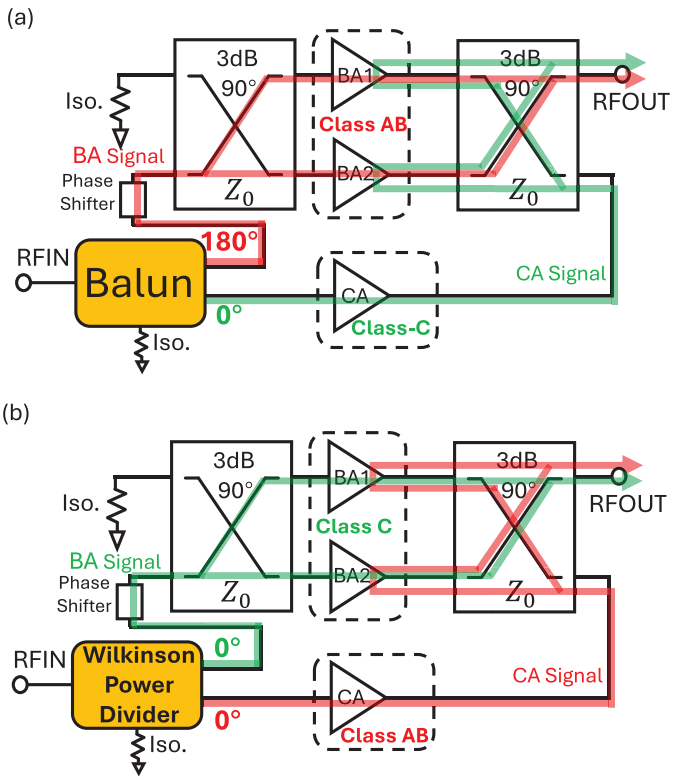

Fig. 1. (a) General circuit schematic of the proposed ultrawideband DL-LMBA architecture. (b) Circuit schematic of PD-LMBA.

While the broadband performance of PD-LMBA has been validated through extensive experiments, researchers have questioned the feasibility of extending the bandwidth of the other LMBA mode, DL-LMBA. By applying the signal-flow-based broadband theory to DL-LMBA, we identified that the broadband phase-alignment condition for DL-LMBA differs from that of PD-LMBA. This distinction ultimately impacts the circuit topology of DL-LMBA, which will be discussed in detail in this section.

A. Broadband Theory for DL-LMBA Based on Signal-Flow Graph

DL-LMBA comprises a BA serving as the carrier PA and a CA acting as the peaking PA, as illustrated in Fig. 1(a). The carrier BA operates continuously across the entire power range of DL-LMBA. As the output power reaches a certain power level (i.e., OBO), the voltage swing of the BA approaches the supply voltage, VDD, indicating that the BA is entering saturation. To reverse the trend of voltage saturation and maintain efficient power delivery, the peaking CA is activated at this power level and begins modulating the impedance seen by the BA to lower values. This enables the PA to continue generating power while maintaining the BA at its maximum voltage swing, thereby sustaining high efficiency over a wide range of power levels. This load modulation mechanism is similar to a DPA [9].

To properly characterize the broadband load modulation behavior of DL-LMBA, the S-matrices of the PA and

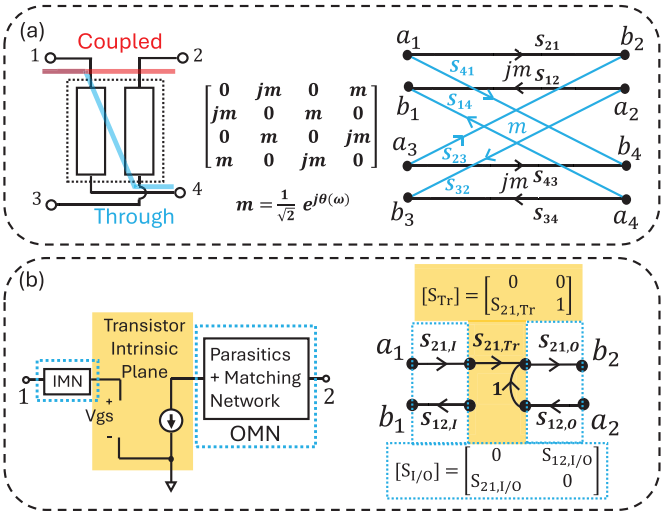

Fig. 2. Circuit schematics, S-matrices, and signal-flow graphs of (a) wideband quadrature coupler and (b) standalone PA in [48].

quadrature coupler, along with their respective signal-flow graphs, are shown in Fig. 2. The full signal-flow graph of DL-LMBA can then be constructed by combining each individual part of the circuit. Using Mason's rule, the signal path for both the BA and CA can be visualized and analyzed, as shown in Fig. 1. From a signal-flow perspective, the load modulation mechanism of LMBA can be explained as follows [48]: when the CA signal propagates toward the intrinsic drain of the BA, it can be viewed as a "reflected" wave, thereby creating a "mismatched" impedance. By varying the amplitude and phase of this "reflected" wave (i.e., the CA signal), the reflection coefficient seen at the BA's intrinsic drain changes accordingly, resulting in a dynamically modulated impedance for the BA. The CA and BA signals are then combined at the BA drain and ultimately propagate together to the output.

By calculating the reflection coefficient at the intrinsic drain of the BA based on the signal-flow graph, the broadband load modulation behavior of LMBA [48] is described by

$$Z_{\mathrm{BA}} = \gamma_{\mathrm{BA}} Z_0 \left[1 + \sqrt{2} \frac{|I_{\mathrm{CA}}|}{|I_{\mathrm{BA}}|} \sqrt{\frac{\gamma_{\mathrm{CA}}}{\gamma_{\mathrm{BA}}}} e^{j(\theta_{\mathrm{CA}}(\omega) - \theta_{\mathrm{BA}}(\omega))} \right] \quad (1)$$

where $|I_{\mathrm{CA}}|$ and $|I_{\mathrm{BA}}|$ represent the magnitudes of the CA and BA currents at the intrinsic drain, respectively. The variations of $|I_{\mathrm{CA}}|$ and $|I_{\mathrm{BA}}|$ across different output power levels for various LMBA modes are illustrated in Fig. 3. Z_{BA} refers to the intrinsic drain impedance of BA. $(\theta_{\mathrm{CA}}(\omega) - \theta_{\mathrm{BA}}(\omega))$ denotes the frequency-dependent phase offset between the CA and BA signal paths at the BA intrinsic drain. γ_{BA} and γ_{CA} represent the impedance transformation ratio of BA and CA OMNs, respectively. These parameters are illustrated in Fig. 4.

Given the ideal load modulation behavior of DL-LMBA, the impedance seen by the BA should have real values. Furthermore, Z_{BA} should decrease as the current ratio $(|I_{\mathrm{CA}}|/|I_{\mathrm{BA}}|)$ increases, which naturally occurs with rising input power due to DL-LMBA's biasing configuration. To achieve this behavior over a broad bandwidth, a negative sign should be introduced in Z_{BA}, which can be expressed as

$$Z_{\mathrm{BA}} = \gamma_{\mathrm{BA}} Z_0 \left(1 - \sqrt{2} \frac{|I_{\mathrm{CA}}|}{|I_{\mathrm{BA}}|} \sqrt{\frac{\gamma_{\mathrm{CA}}}{\gamma_{\mathrm{BA}}}} \right). \quad (2)$$

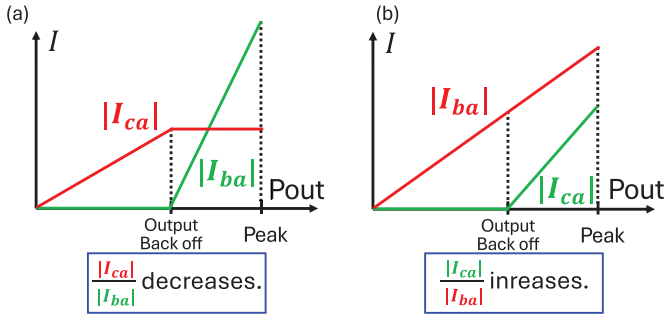

Fig. 3. Current profile of (a) PD-LMBA and (b) DL-LMBA.

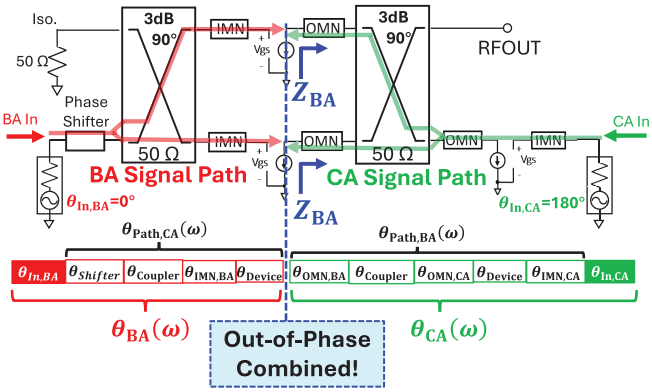

Fig. 4. Full signal-flow graph of DL-LMBA showing BA (in red) and CA (in green) signal paths.

By comparing (1) and (2), the negative sign in (2) requires the following phase-alignment condition to hold:

$$|\theta_{\mathrm{CA}}(\omega) - \theta_{\mathrm{BA}}(\omega)| = 180^\circ. \quad (3)$$

While the original LMBA theory [19], [24] only applies for a single frequency, (2) incorporates the effects of MNs, couplers and transistors, which is valid across the entire operating bandwidth of DL-LMBA. As indicated by (3), the BA and CA signals should ideally combine out of phase at the intrinsic drain of the BA across all frequencies, as illustrated in Fig. 4, to ensure that the second term in (2) retains a negative sign. Combined with an increasing current ratio $(|I_{\mathrm{CA}}|/|I_{\mathrm{BA}}|)$, as shown in Fig. 3(b), this results in a desirable reduction in Z_{BA}, thereby enabling the intended load modulation.

Practically, achieving a constant 180° phase offset between the CA and BA paths depends on both the phase response of the MNs and the phase offset introduced by the input power divider. To clarify the broadband phase-alignment condition for the DL-LMBA, the total phase of each path can be decomposed, as shown in Fig. 4

$$\begin{aligned} \theta_{\mathrm{CA}}(\omega) &= \theta_{\mathrm{In,CA}}(\omega) + \theta_{\mathrm{Path,CA}}(\omega) \\ \theta_{\mathrm{BA}}(\omega) &= \theta_{\mathrm{In,BA}}(\omega) + \theta_{\mathrm{Path,BA}}(\omega) \end{aligned} \quad (4)$$

where $\theta_{\mathrm{In,CA}}(\omega)$ and $\theta_{\mathrm{In,BA}}(\omega)$ denote the phase shifts introduced by the input power divider to the CA and BA paths, respectively. The remaining terms, $\theta_{\mathrm{Path,CA}}(\omega)$ and $\theta_{\mathrm{Path,BA}}(\omega)$, account for the total phase delay contributed by all subsequent building blocks along the BA and CA paths, including the MNs and couplers.

Since the MNs are primarily designed to provide impedance matching, their phase delay response is typically less

controllable (which is also highly frequency dependent). Therefore, to ensure the desired constant phase offset across a wide bandwidth, one viable solution is to impose a fixed phase offset through the input power divider. In this work, we assume the following input phase condition to realize the 180° offset:

$$\left|\theta_{\text{In,CA}}(\omega) - \theta_{\text{In,BA}}(\omega)\right| = 180°. \tag{5}$$

Given this assumption, achieving the overall 180° phase offset at the intrinsic drains requires that the remaining signal paths have equal phase delays

$$\theta_{\text{Path,CA}}(\omega) = \theta_{\text{Path,BA}}(\omega). \tag{6}$$

This condition can be achieved in practice. For instance, when the MNs are implemented using transmission lines, their phase responses can be closely matched by adopting topologies with minimal shunt stubs in both paths and utilizing a linear phase shifter, as demonstrated in [48].

On the other hand, in a PD-LMBA, as illustrated in Fig. 1(b), where the CA functions as the carrier and the BA as the peaking amplifier, a constant phase offset of 0° between the BA and CA signal paths is desired [48]. This ensures in-phase signal combination at the BA drain, resulting in a "+" sign for the second term in (2). Combined with a decreasing current ratio ($|I_{\text{CA}}|/|I_{\text{BA}}|$) as the input power increases, illustrated in Fig. 3(a), this drives Z_{BA} lower, thereby achieving the intended load modulation. This fundamental difference in phase-alignment requirements ultimately affects the circuit design, particularly in the selection of power dividers and MNs, depending on the mode of LMBA.

B. Verification of the Phase-Alignment Condition of DL-LMBA With Different Power Dividers

In previously reported LMBAs, the power divider has been implemented using various methods, including quadrature couplers [22], [52], Wilkinson power dividers [26], [30], [32], [39], [40], and baluns [53]. For achieving a constant 180° phase offset, two main options are available: baluns and 180° hybrid couplers. For broadband operation of DL-LMBA, using other types of power dividers (e.g., quadrature couplers and Wilkinson power dividers) requires adding or removing a transmission line with an electrical length of 90° or 180° to enforce the 180° phase offset at the center frequency. Unfortunately, the phase shift introduced by such transmission lines is inherently frequency dependent. When a 180° line is combined with a broadband Wilkinson power divider, for example, the resulting network behaves as a narrowband "balun." This is because the frequency-dependent phase delay of the transmission line introduces substantial phase error, especially at frequencies far from the center, thereby degrading the desired constant phase offset critical for broadband DL-LMBA operation.

To verify the impact of different power dividers on the broadband load modulation behavior of DL-LMBA, an ideal broadband DL-LMBA model is constructed using advanced design system (ADS), as shown in Fig. 5, following a similar approach as in [48]. The MNs are implemented using ideal 50-Ω transmission lines, and the power divider is modeled

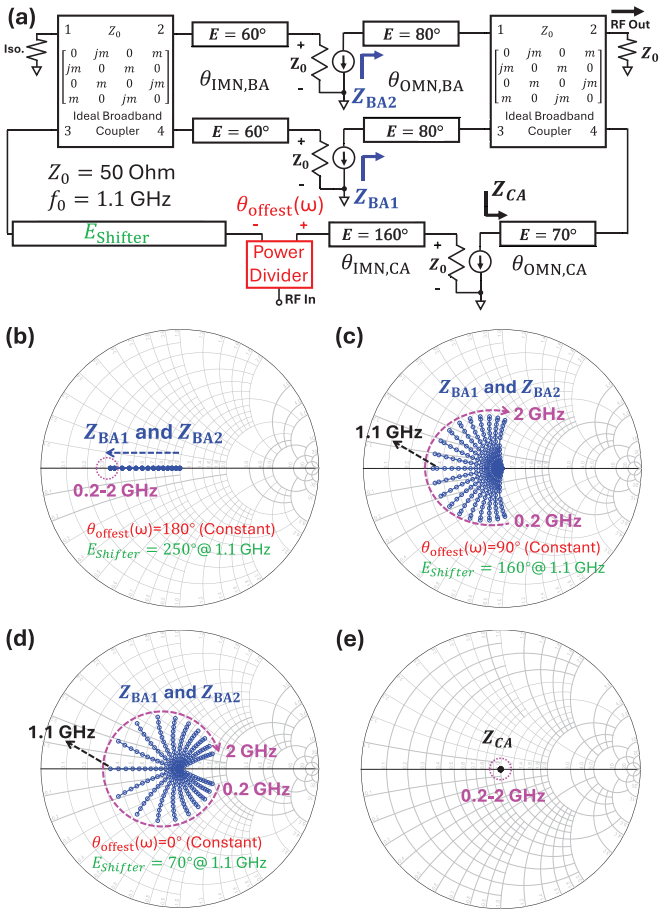

Fig. 5. (a) Circuit schematic of an ideal DL-LMBA with transmission-line-based MNs and phase shifter. Load trajectories of BA when using (b) ideal broadband 180° power divider (e.g., balun), (c) ideal broadband 90° power divider (e.g., quadrature coupler), and (d) ideal broadband 0° power divider (e.g., Wilkinson power divider). (e) Load impedance of CA.

using two separate power sources with a specific phase offset, $\theta_{\text{offset}}(\omega)$. The electrical length of each transmission line at 1.1 GHz is also indicated in Fig. 5(a). The electrical lengths of the MNs can be chosen with considerable flexibility, as long as the phase alignment condition given by (3) is satisfied. Once these MNs are defined, the electrical lengths of the phase shifter and the input power divider must be properly configured to maintain a consistent 180° phase offset between the BA and CA signal paths. This phase alignment requirement, as indicated by (3), can be further expressed through the following relationship:

$$\begin{aligned}\Big|\theta_{\text{Offset}}(\omega) + \theta_{\text{IMN,CA}}(\omega) + \theta_{\text{OMN,CA}}(\omega) + \theta_{\text{OMN,BA}}(\omega) \\ -\theta_{\text{IMN,BA}}(\omega) - \theta_{\text{Shifter}}(\omega)\Big| = 180°\end{aligned} \tag{7}$$

where $\theta_{\text{Offset}}(\omega)$ denotes the constant phase offset introduced by the broadband power divider, and the remaining terms represent the frequency-dependent phase delays contributed by the MNs and the phase shifter. Note that the phase delay introduced by the coupler is identical in both paths and therefore cancels out in (7).

The ideal DL-LMBA model is simulated from 0.2 to 2 GHz with an increasing ratio of ($|I_{\text{CA}}|/|I_{\text{BA}}|$), and the trajectories of

Z_{BA} are depicted in Fig. 5(b)–(d) for different power dividers. The electrical length of the phase shifter is then determined based on (7) to satisfy the required phase condition. The CA impedance at the intrinsic drain, Z_{CA}, is plotted in Fig. 5(e), where it remains constant at $50-\Omega$ due to the absence of load modulation.

When a 180° power divider (e.g., a balun) is used, consistent load modulation behavior is observed across the entire bandwidth, as shown in Fig. 5(b), where (7) is satisfied at all frequencies. In contrast, when a 90° power divider (e.g., a quadrature coupler) is used and a 90° line is removed from the phase shifter, ideal load modulation can only be achieved at the center frequency, as illustrated in Fig. 5(c). Furthermore, using a 0° power divider (e.g., a Wilkinson power divider) results in even poorer bandwidth performance in Fig. 5(d), as a longer transmission line (i.e., 180°) must be added or removed to achieve the desired phase offset, leading to greater variation in electrical length over frequency. Notably, this systematic error cannot be corrected simply by adjusting the length of the phase shifter. On the other hand, for ultrabroadband PD-LMBA operation, a Wilkinson power divider provides the widest bandwidth when no special phase-shifting circuits are employed, as demonstrated in [48], whereas a balun generally yields the poorest bandwidth performance.

Since the 180° power divider is relatively more challenging to implement and may occupy a larger area, a broadband quadrature coupler may be preferred in certain applications due to its ease of implementation, moderate bandwidth, and the potential to absorb a 90° line into the quadrature coupler. It is also important to emphasize that a 180° power divider is not strictly required for achieving ultrabroadband DL-LMBA operation. A constant 180° phase offset can alternatively be realized using other phase-shifting topologies, which are beyond the scope of this article and thus not discussed for the sake of simplicity. Furthermore, the optimal choice of power divider depends on the overall phase-delay response of the PA's MNs. Therefore, multiple power divider options should be evaluated in conjunction with the PA design to identify the configuration that offers the best performance for load-modulated PAs.

III. Novel Broadband All-Port-Matched Balun

As discussed in Section II, the condition described by (3) leads to ultrabroadband DL-LMBA operation. Although the traditional balun [54] might appear suitable for providing a constant 180° phase offset, the authors are unable to implement an ultrawideband DL-LMBA using a nonall-port-matched balun due to mismatches between the balun's two output ports. This section discusses the necessity of using an all-port-matched balun and presents the theory and design of the proposed broadband all-port-matched balun.

A. Comparison Between Matched and Unmatched Baluns

Generally, a balun can maintain a constant 180° phase offset as long as the two output ports have identical impedances (even if mismatched). This condition is met when two identical circuits (e.g., two identical transistors in a differential pair) are connected to each output port [55]. However, in DL-LMBA architecture shown in Fig. 1, one output port of the power divider connects to a quadrature coupler, which provides a constant $50-\Omega$ impedance regardless of the BA IMN's mismatch, while the other output port connects directly to the CA IMN, encountering a highly mismatched impedance—an unavoidable factor in broadband designs. This mismatch between the balun's output ports prevents it from maintaining a constant 180° phase offset across frequencies, leading to significant amplitude and phase error.

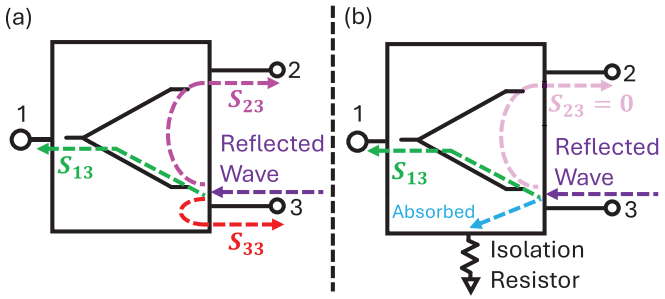

Fig. 6. Comparison between (a) nonall-port-matched balun and (b) all-port-matched balun.

In contrast, a 180° hybrid coupler or an all-port-matched balun offers greater robustness to mismatches at its output ports, primarily due to the inclusion of an isolation resistor. This enhanced mismatch resilience can be explained as follows: in an unmatched balun, when a signal is applied at port 1 and a mismatch occurs at port 3, as illustrated in Fig. 6(a), a portion of the reflected signal (approximately half) propagates back toward the input, due to the reciprocity of the circuit. The remaining portion splits between port 2 and further reflections, causing significant amplitude and phase error at port 2.

When an isolation resistor is incorporated into the circuit, the balun becomes matched at all ports. This resistive element is critical, as a three-port network cannot simultaneously be lossless, reciprocal, and matched at all ports [56]. Under this configuration, if a mismatch occurs at port 3, half of the reflected signal still propagates to the input, while the other half is fully absorbed by the isolation resistor, as depicted in Fig. 6(b). By absorbing the reflected wave, the isolation resistor prevents the reflected wave's propagation to port 2 (i.e., $S_{23} = 0$), thereby mitigating amplitude and phase imbalance at the balun output for mismatched case.

While the authors identified a commercially available nonall-port-matched balun capable of covering a decade bandwidth, as discussed before, its performance is compromised when interfaced with LMBA due to the mismatch between its two output ports. Furthermore, due to limitations in bandwidth, power handling, and cost, no commercially available 180° hybrid coupler or all-port-matched balun is suitable for the ultrawideband DL-LMBA prototype. To overcome these challenges, we propose a novel RPB in our conference paper [51], the operating principles of which will be discussed in detail in Sections III-B and III-C.

B. Revisiting RTPS Through Signal-Flow Graph

The general schematic of a reflective-type phase shifter (RTPS) is shown in Fig. 7(a). Port 1 serves as the input,

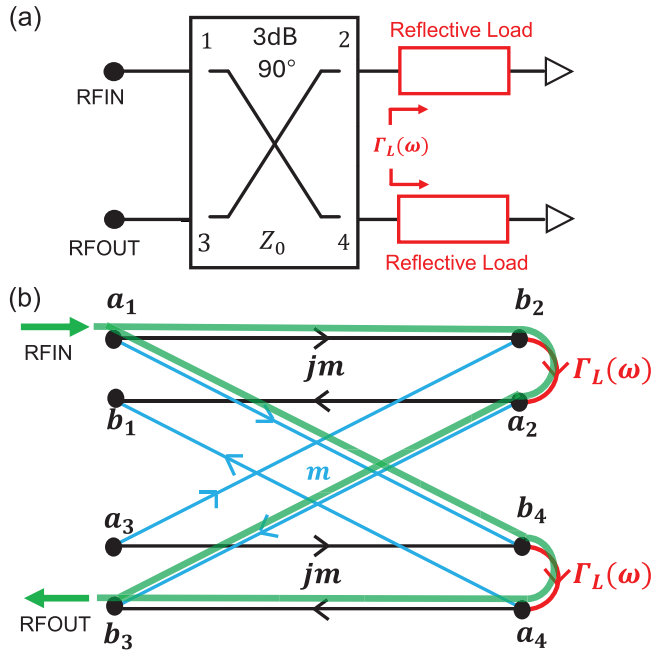

Fig. 7. (a) Circuit schematic and (b) signal-flow graph of a RTPS based on broadband coupler.

while both the thru and coupled ports are terminated with the same reflective load, $\Gamma_L(\omega)$. The isolation port functions as the output of the phase shifter. Existing theories of RTPS are typically limited to single-frequency analysis [57], [58], [59], in which the frequency-dependent phase delay of the coupler is not accounted for in the analytical equations. To better understand the behavior of RTPS over a broad bandwidth and to offer a visual and intuitive explanation of the phase-shifting mechanism, we adopt a signal-flow-based approach. Specifically, we utilize the broadband S-matrix and the corresponding signal-flow graph of a quadrature coupler [48], as indicated by Fig. 7(b).

Using Mason's Rule [56], the signal paths can be identified and visualized in Fig. 7(b). Initially, the input signal at node a_1 is split equally, with half of the signal propagating toward port 2 and the other half toward port 4. Upon reaching the reflective loads, the signals are reflected back through ports 2 and 4 and subsequently recombined at the output node b_3. The gain of this signal path can be calculated as follows:

$$b_3 = a_1 \cdot 2jm^2\Gamma_L(\omega) \tag{8}$$

where m (i.e., S_41) $= (1/(2)^{1/2})e^{j\theta_{\text{Coupler}}(\omega)}$. The magnitude of m is $(1/(2)^{1/2})$, indicating an equal power split between the through port and the coupled port. The phase of m, denoted by $\theta_{\text{Coupler}}(\omega)$, captures the frequency dependence of the coupler. Despite this, the relationship $S\_21 = jS_{41}$ remains valid across the entire frequency band, implying that the coupler is assumed to exhibit zero phase error over frequency [48]. For the reflected wave at the input port, b_1, although portions of the signal are reflected from ports 2 and 4, they cancel perfectly at node b_1 due to having equal magnitudes and a 180° phase difference. In other words, RTPS is matched throughout the bandwidth of the coupler. Notably, this signal-flow behavior closely resembles that of LMBA [48].

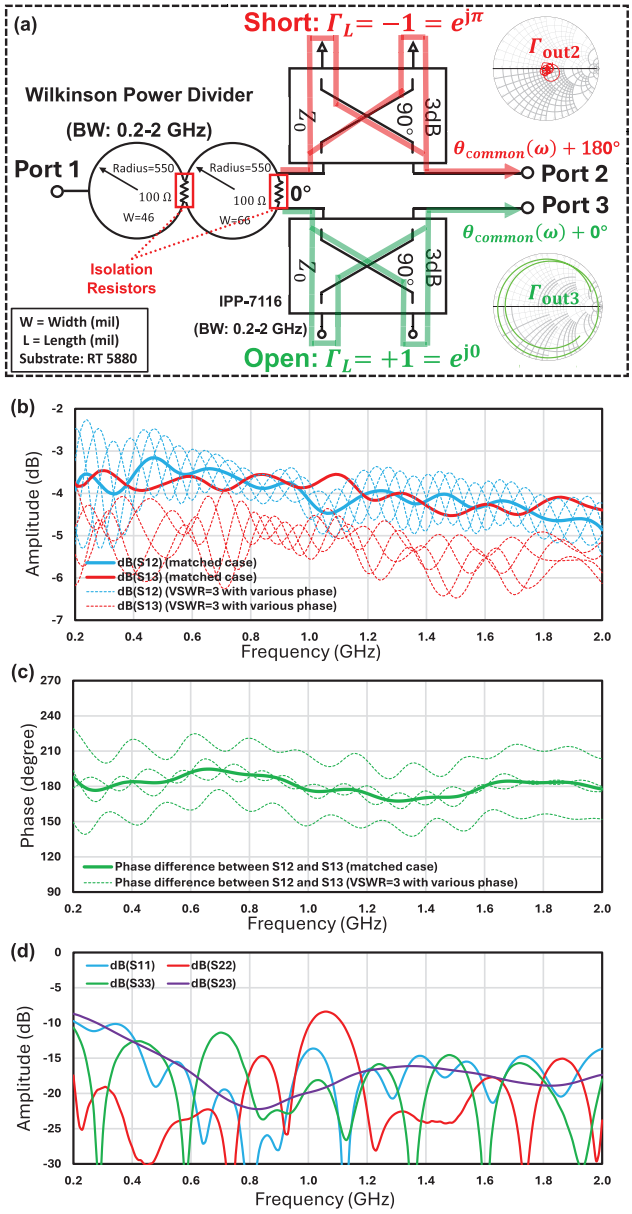

Fig. 8. (a) Circuit schematic of the proposed RPB. Simulation results: (b) amplitude imbalance and (c) phase imbalance, under matched and mismatched cases (VSWR = 1 for port 2 and VSWR = 3 for port 3 with $\angle\Gamma_{\text{out3}} = 0°, 90°, 180°$, and 270°). (d) Simulated return loss and isolation.

Based on (8), the phase shift provided by RTPS is given by

$$\theta_{\text{RTPS}}(\omega) = 2\theta_{\text{Coupler}}(\omega) + 90° + \angle\Gamma_L(\omega) \tag{9}$$

where $\theta_{\text{Coupler}}(\omega) = \angle S_{41}$. The first two terms of (9) indicate the phase shift induced by the coupler, and θ_{coupler} can be roughly viewed as a linear function of frequency [48]. The last term in (9) represents the phase shift introduced by the reflective load, which is typically implemented using varactor-based circuits to achieve a wide phase tuning range.

C. Analysis and Design of Novel Broadband All-Port-Matched Balun

The circuit schematic of the proposed RPB is shown in Fig. 8(a), which consists of a Wilkinson power divider and two quadrature couplers, each functioning as a RTPS. We

demonstrate, for the first time, that by terminating the reflective ports of the two quadrature couplers with a short and an open, respectively, a constant 180° phase offset can be achieved over a decade bandwidth. By adopting identical couplers for both signal paths, the frequency-dependent phase delay introduced by the coupler, $\theta_{\text{common}}(\omega)$, corresponding to the first two terms in (9), is effectively canceled out within the coupler's bandwidth. This cancellation is a key feature that enables broadband operation. The Wilkinson power divider splits the input signal into two identical outputs, while the phase shifters introduce the required 180° phase offset. This phase difference between the two signal paths arises solely from the difference in their respective reflective terminations

$$\Gamma_{\text{L,short}} = e^{j\pi}$$
$$\Gamma_{\text{L,open}} = e^{j0}. \tag{10}$$

Since "short" and "open" terminations can be naturally implemented with very broad bandwidths, the 180° phase offset can be consistently maintained across the entire band. This broadband performance is achievable as long as both the Wilkinson power divider and the quadrature couplers provides sufficient bandwidth. The proposed RPB is matched at all ports, as both the Wilkinson power divider and RTPS are all-port-matched components. Furthermore, the RPB is intrinsically robust to mismatches between its output ports, as the Wilkinson power divider includes an isolation resistor to absorb reflected waves.

Fig. 8(b) and (c) show the amplitude and phase imbalance under matched and mismatched conditions, respectively. In the matched case, the proposed 180° power divider exhibits an insertion loss of approximately 1–1.5 dB, which includes the inherent 1-dB loss from the coupler. Fig. 8(b) also shows frequency-dependent variations in amplitude imbalance, which are primarily influenced by the performance of the coupler-based phase shifter (i.e., the amplitude and phase imbalances of the quadrature couplers). Therefore, careful design or selection of these couplers is essential to minimize such nonidealities. The phase imbalance remains within approximately ±10° over the 0.2–2 GHz frequency range. Under mismatched conditions (with VSWR = 3 at port 3), the phase imbalance increases to around ±30°. Fig. 8(d) presents the return loss at each port and the isolation between ports 2 and 3. All S-parameters remain below −10 dB across most of the bandwidth. To make a fair comparison between the proposed balun and a nonall-port-matched balun, the amplitude and phase imbalance under a mismatched condition are shown in Fig. 9(a) and (b). Compared to the commercially available unmatched balun (IPP-5001), the proposed RPB exhibits less variation in both amplitude and phase when subjected to a 3:1 VSWR (with various phases) at port 3 across the band. This result demonstrates that the RPB effectively mitigates mismatch effects between its output ports by partially absorbing reflected waves through the isolation resistor.

IV. Design of Decade-Bandwidth DL-LMBA

To validate the proposed theory, three 10-W GaN transistors (MACOM CG2H40010F) are used to implement the BA and CA. The schematic of the realized ultrawideband DL-LMBA

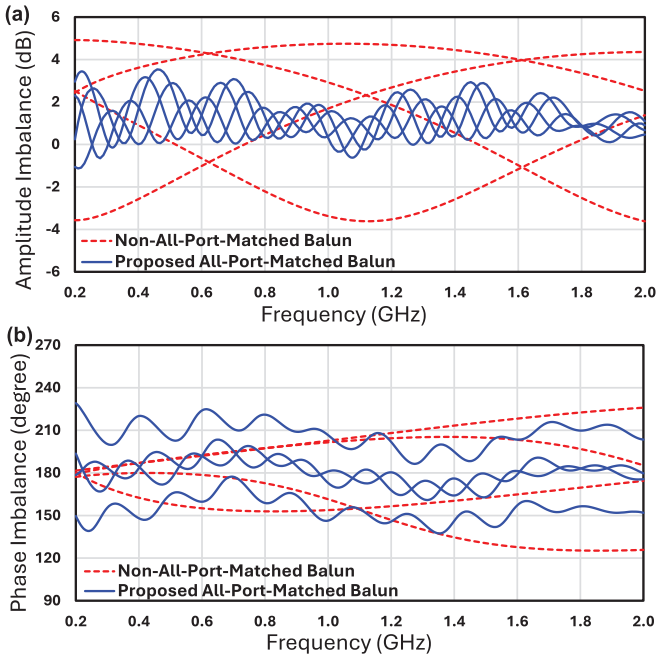

Fig. 9. Comparison between matched and nonall-port-matched baluns under 3:1 VSWR, showing (a) amplitude imbalance and (b) phase imbalance. The mismatch scenario assumes VSWR = 1 at port 2 and VSWR = 3 at port 3 with $\angle\Gamma_{\text{out3}}$ = 0°, 90°, 180°, and 270°.

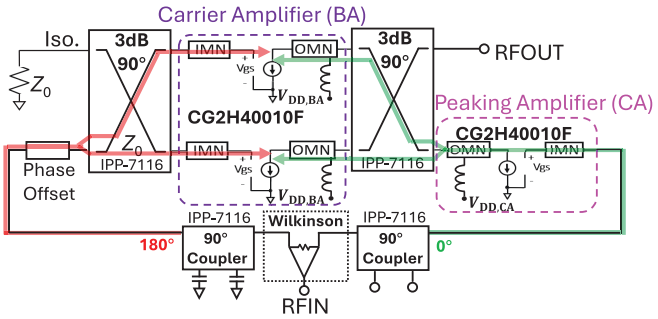

Fig. 10. Circuit schematic of the ultrabroadband DL-LMBA prototype.

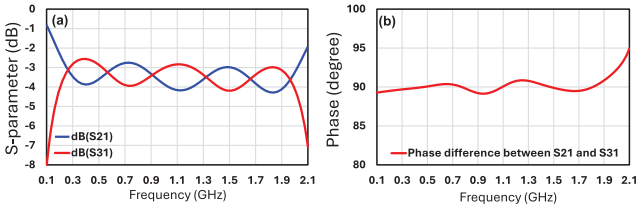

Fig. 11. (a) Amplitude and (b) phase of IPP-7116 from 0.2 to 2 GHz.

circuit is shown in Fig. 10. The target OBO is set to 6-dB, with a frequency range spanning 0.2 to 2 GHz. Two identical 50−Ω wideband couplers (IPP-7116, innovative power products) are employed at the input and output of the BA to cover the frequency range from 0.2 to 2 GHz as well as provide the same phase delay for both BA and CA signal paths. To achieve a decade-wide bandwidth for the RPB, a two-section Wilkinson power divider is used in conjunction with two IPP-7116 couplers, as shown in Fig. 8(a). Within the bandwidth of IPP-7116 from 0.2 to 2 GHz, the amplitude imbalance is around 1-dB, and the phase imbalance is less than 3°, as shown in Fig. 11. The circuit is electromagnetically

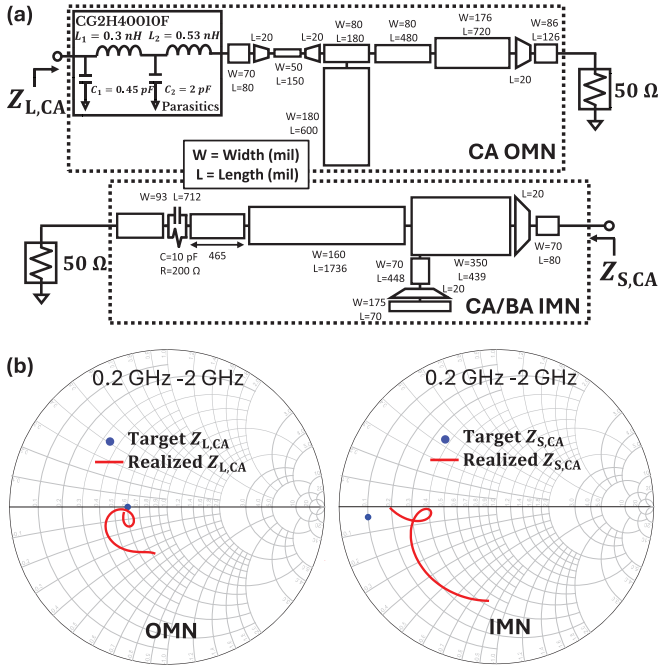

Fig. 12. (a) Circuit schematic of CA OMN and IMN [48]. (b) Simulated results of CA.

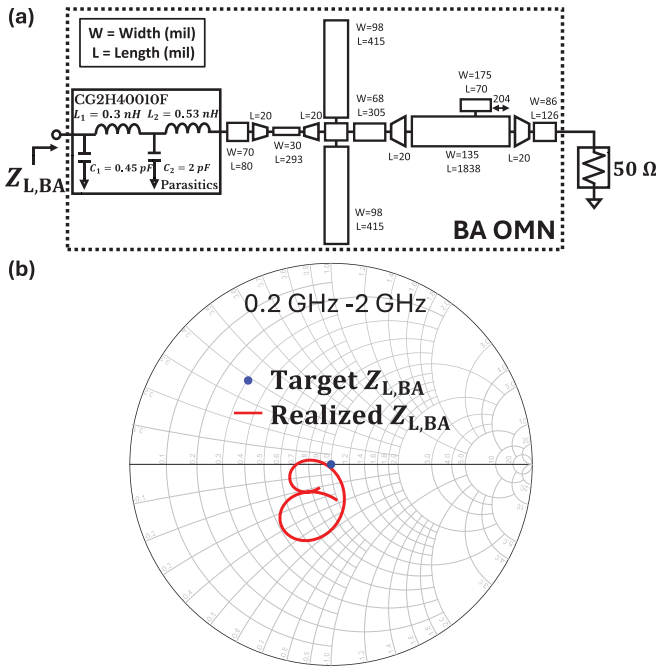

Fig. 13. (a) Circuit schematic of BA OMN. (b) Simulated matching results of BA.

(EM) simulated in ADS based on a 31-mil thick Rogers Duroid-5880 PCB board with a dielectric constant of 2.2.

A. Ultrabroadband CA and BA Design

The prototype of DL-LMBA employs the same IMN and OMN for the CA as reported in [48], since both designs share an identical operating frequency range. The schematics and dimensions of the CA's IMN and OMN are shown in Fig. 12(a) [48]. The target intrinsic drain impedance for the CA's OMN is set to 30Ω. The extracted device parasitics [48] are included in the OMN design, and the EM simulation results are presented in Fig. 12(b). For the IMN, the optimum impedance, acquired from source-pull simulations, is 5—2j, and the simulated source impedance is illustrated in Fig. 12(b), which also includes the RC stability network.

For the BA design, the IMN adopts the same topology as the CA IMN to ensure similar broadband matching characteristics. However, the OMN of the BA is carefully engineered to accommodate the unique load modulation behavior of the DL-LMBA architecture. Specifically, when the peaking amplifier (i.e., CA) turns on at the back-off power level, the impedance at the BA decreases below $\gamma_{BA}Z_0$, as described by (2). To achieve a higher OBO range, the impedance must be modulated to increasingly lower values as the output power rises. This behavior can result in a significant deviation from the optimum impedance, thereby degrading efficiency.

This challenge is particularly pronounced for high-power packaged GaN transistors, where the optimum impedance typically lies in the range of 30–100 Ω, depending on the power and voltage settings. To counteract the low peak-power impedance resulting from the DL-LMBA's load modulation behavior, it is highly desirable to use a transistor with a low optimum impedance in combination with an OMN that provides a high impedance transformation ratio, γ_{BA} [30]. However, achieving a high transformation ratio across a decade bandwidth is extremely challenging, especially when the OMN must also absorb transistor parasitics. In practice, we found that a transformation ratio of 50 : 50 Ω (i.e., $\gamma_{BA} = 1$) is the highest achievable impedance for the OMN of the CG2H40010F transistor, given the constraints of the target bandwidth. The corresponding OMN circuit is shown in Fig. 13(a), and the EM simulation results are presented in Fig. 13(b).

To further accommodate the low peak-power impedance, a supply voltage of $V_{DD,BA}$ = 15 V is used instead of the nominal 28 V. This adjustment helps lower the transistor's optimum impedance without significantly sacrificing output power or gain. However, these measures alone are insufficient to fully resolve the low-impedance issue. An additional design strategy is required, which will be discussed in Section IV-B.

B. Ultrabroadband Phase Alignment

To satisfy the phase-alignment condition and minimize amplitude and phase errors, a decade-bandwidth, all-port-matched balun is proposed and implemented, as detailed in Section III. Furthermore, the IMNs and OMNs for both the BA and CA are designed with a minimal number of shunt stubs to reduce phase dispersion, thereby simplifying the phase-alignment requirement [48]. To further address the low-impedance issue, the phase shifter is intentionally configured to modulate the intrinsic BA load trajectories into the inductive region, avoiding the low-impedance region along the real axis on the Smith chart, as illustrated in Fig. 14(b). These impedance trajectories are plotted based on the intrinsic voltage and current obtained from the foundry model. The "short" reflective termination in the proposed RPB is implemented

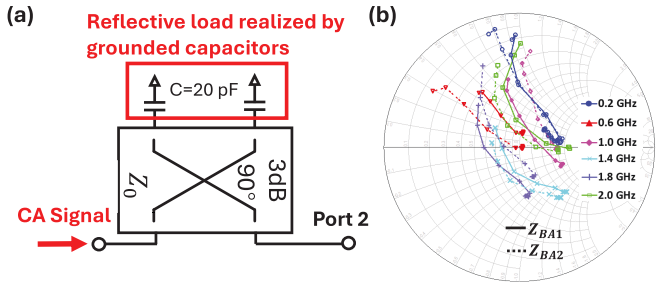

Fig. 14. (a) RTPS configuration for the CA signal path in the proposed RPB. (b) Simulated intrinsic impedance trajectories of the BA across the band.

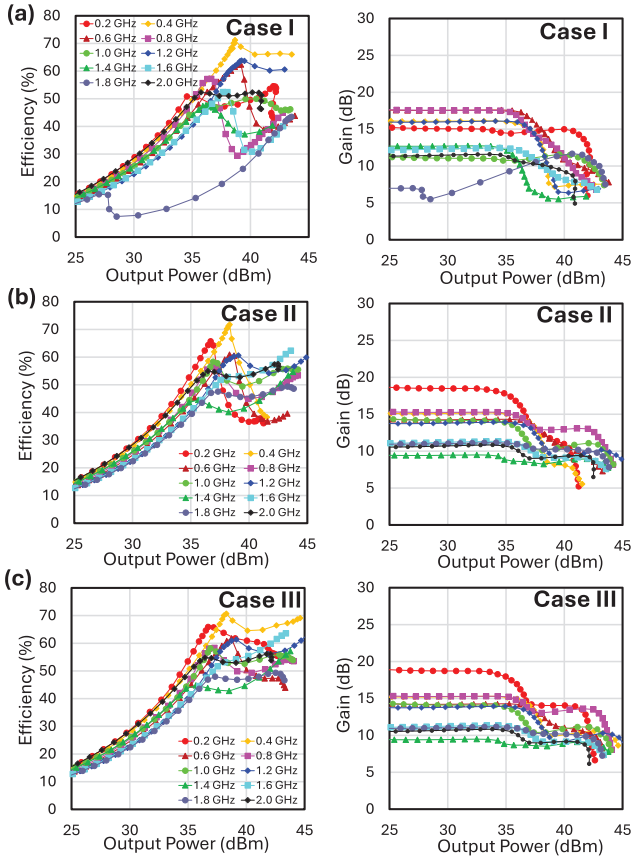

Fig. 15. Simulated efficiency and gain across the band when different balun configurations are used: (a) nonall-port-matched balun, (b) proposed RPB with ideal short termination, and (c) proposed RPB with grounded capacitors as the short termination.

using grounded 20-pF capacitors, as shown in Fig. 14(a), to compensate for the low-frequency phase error caused by mismatches between the RPB's output ports, thereby enhancing the low-frequency performance of DL-LMBA.

To demonstrate the benefits of the proposed DL-LMBA architecture, a comparison is carried out among three cases: Case I, where a commercially available nonall-port-matched balun is used; Case II, where the proposed RPB is implemented with an ideal short termination; and Case III, where the RPB uses grounded 20-pF capacitors to realize the "short" termination. The simulated efficiency and gain curves for these configurations are shown in Fig. 15.

As illustrated in Fig. 15(a), the use of a nonall-port-matched balun in Case I introduces significant amplitude and phase errors, which substantially degrade the gain and efficiency

TABLE I
COMPARISON AMONG CASES I–III (SIMULATED)

Case	P_{max} (dBm)	$Gain$ @ P_{max}(dB)	$Gain$ @ OBO(dB)	DE @ P_{max} (%)	DE @ OBO (%)	OBO (dB)
I	40.9-43.5	5.5-14.3	7.0-17.6	43.5-66.0	14.2-70.1	6
II	41.0-44.5	7.7-12.6	9.24-18.6	36.7-62.3	42.6-61.9	6
III	**42.1-44.7**	**8.75-13.1**	**9.41-18.8**	**46.6-69.1**	**43.9-70.7**	**6**

of the PA. Specifically, the amplitude error leads to highly frequency-dependent and uneven power distribution between the BA and CA, and the phase error disrupts load modulation. These factors induce highly nonconsistent efficiency curves and nonlinear gain response across different power levels, especially at 1.8 GHz, as indicated by Fig. 15(a). In contrast, Case II [see Fig. 15(b)] shows that the gain and efficiency curves become more consistent across different power levels due to reduced amplitude and phase error. However, performance at lower frequencies remains suboptimal, especially in terms of peak power and efficiency. Finally, in Case III [see Fig. 14(c)], replacing the ideal short with grounded 20-pF capacitors yields a significant performance boost across the entire band compared to previous cases. This modification is particularly effective in the 0.2–0.6 GHz range, where both peak power and efficiency are substantially improved. The back-off efficiency remains almost unchanged compared to Case II, as the additional capacitors influence the load modulation behavior only when the CA is turned on.

Note that in all cases, the phase shifter is already tuned for optimal performance, ensuring that the observed differences arise solely from the type of balun implementation rather than suboptimal phase shifter. The phase shifter is primarily optimized for improved efficiency, with gain and output power being secondary considerations. Table I summarizes the performance in terms of output power, gain, and efficiency at both peak power and OBO. Among the three cases, Case III demonstrates a significant improvement across all metrics, highlighting the effectiveness of the proposed balun configuration.

C. Overall Schematic and Simulation Results

The overall circuit schematic is shown in Fig. 16. The physical dimensions of the MNs and power divider have been presented in previous sections. For PA biasing, high-Q inductors (Coilcraft 1515SQ-68N) are used, along with several dc-blocking capacitors. The BA is biased in Class-AB with a drain voltage, $V_{DD,BA}$, of 15 V, while the CA is biased in Class-C with $V_{DD,CA}$ = 30 V. The CG2H40010F transistor is selected for the BA due to its relatively low optimum impedance and acceptable parasitic parameters. Additionally, the gate bias voltages (V_{GS}) are tuned to optimize PA performance across the frequency range. Fig. 15(c) presents the EM simulated gain and efficiency of DL-LMBA, demonstrating pronounced broadband load modulation behavior and efficiency enhancement.

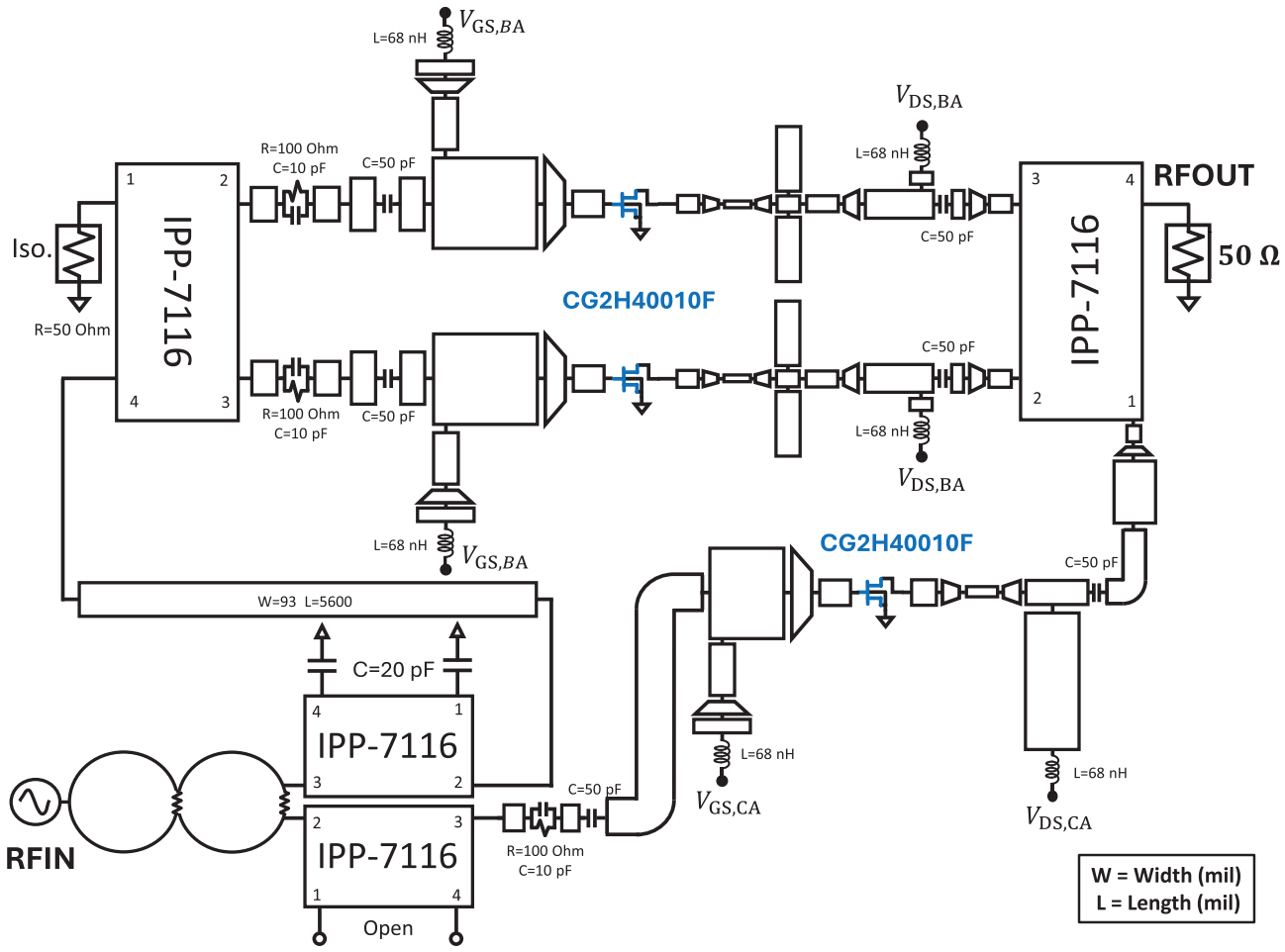

Fig. 16. Full circuit schematic of decade-bandwidth DL-LMBA.

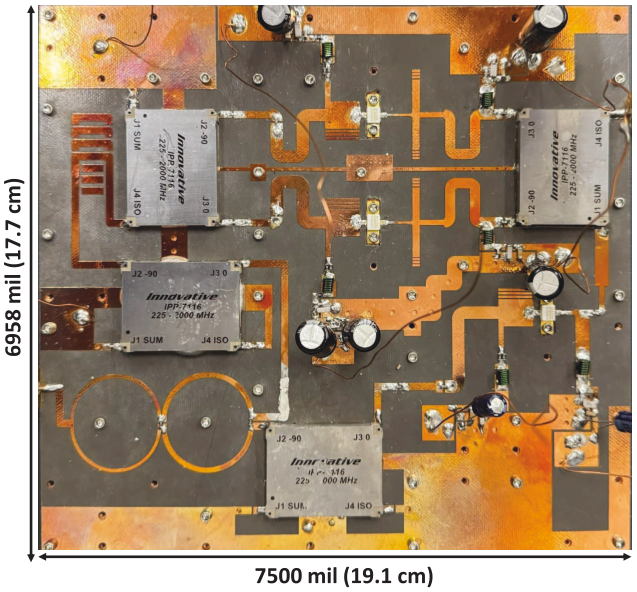

Fig. 17. Fabricated DL-LMBA prototype.

The circuit shown in Fig. 17 occupies a relatively large area, primarily due to the customized balun and the wide target bandwidth. Therefore, a discussion on potential size reduction is provided here. The bandwidth of couplers and baluns can be extended by cascading multiple sections, a necessary condition in the broadband DL-LMBA design. However, this inevitably increases circuit area. In our implementation, an all-port-matched balun is essential due to the high VSWR at the CA input, which further contributes to the area overhead. To reduce the overall size of the balun, one option is to target a narrower bandwidth (e.g., 3:1), which can allow for simpler balun structures without the need for cascading. Furthermore, broadband all-port-matched baluns can be realized more compactly using multilayer PCB technologies [60], [61], providing a more area-efficient solution.

V. Implementation and Experimental Results

The PA is implemented on a 31-mil thick Rogers Duroid-5880 PCB board with a dielectric constant of 2.2, and the realized circuit is shown in Fig. 17. The prototype is tested using both continuous-wave (CW) and modulated signals.

A. Continuous-Wave Measurement

The DL-LMBA prototype is evaluated using a single-tone signal across the frequency range of 0.2 to 2 GHz at various power levels. The frequency response is compared with simulation results, as shown in Fig. 18. A peak output power ranging from 41–44 dBm is observed across the entire bandwidth, along with a gain of 8–17 dB at different

TABLE II
COMPARISON WITH STATE-OF-THE-ART OF WIDEBAND LOAD-MODULATED PAS

Ref. / Year	Mode	Freq. (GHz)	f_{high}/f_{low}	$Gain$ (dB)	P_{max} (dBm)	DE @ P_{max} (%)	DE @ OBO (%)	OBO (dB)
[9] 2018	DPA	1.5-3.8	2.5	10-14	42-43	42-63	33-55	6
[45] 2024	SLCG	1-3	3	8.2-11.2	36.5-38.7	47.8-57.7	45.4-51.2	6
[24] 2020	PD-LMBA	1.5-2.7	1.8	8-12	43	58-72	47-58	10
[26] 2021	PD-LMBA	0.55-2.2	4	8-17*	41-43	49-82	39-64	10
[28] 2023	SLMBA	2.05-3.65	1.8	8-11	45-47	61-80	51-66	10
[25] 2020	SLMBA	3.05-3.55	1.16	9.5-10.3	42.3-43.7	60.8-74.8	43.2-51.4	10
[48] 2025	PD-LMBA	0.2-2	10	9-15	43-45	51-72	44-62	10
[21] 2018	Dual-Input DL-LMBA	1.7-2.5	1.5	10-13*	48-49	51-61*	45-56*	6
[22] 2017	DL-LMBA	1.8-3.8	2.1	8*	44	46-70	33-49	6
[30] 2020	DL-LMBA	1.45-2.45	1.7	11-13	46-47	67-78	46-57	6
This work	**DL-LMBA**	**0.2-2**	**10**	**8-17**	**41-44**	**44-67**	**43-75**	**6**

*Graphically estimated

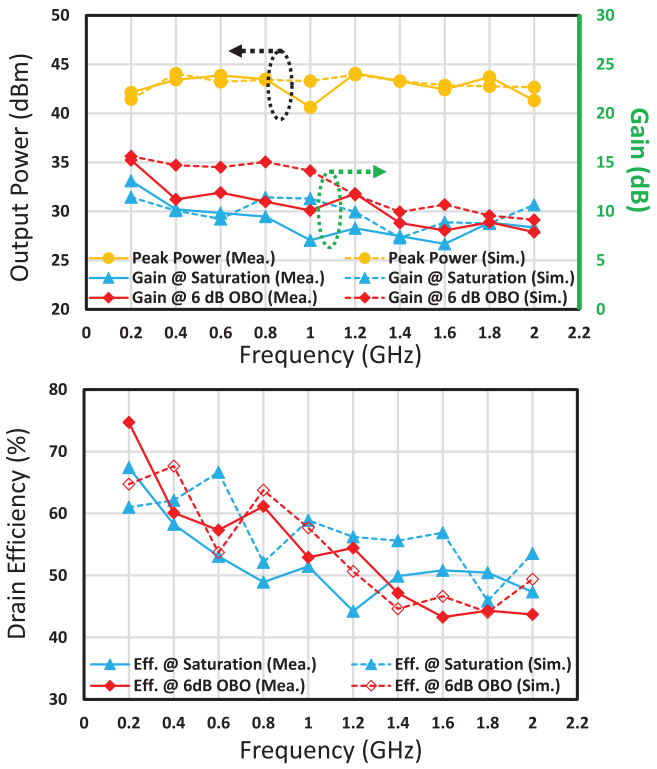

Fig. 18. Measured versus simulated output power, gain, and efficiency at various power levels from 0.2 to 2 GHz.

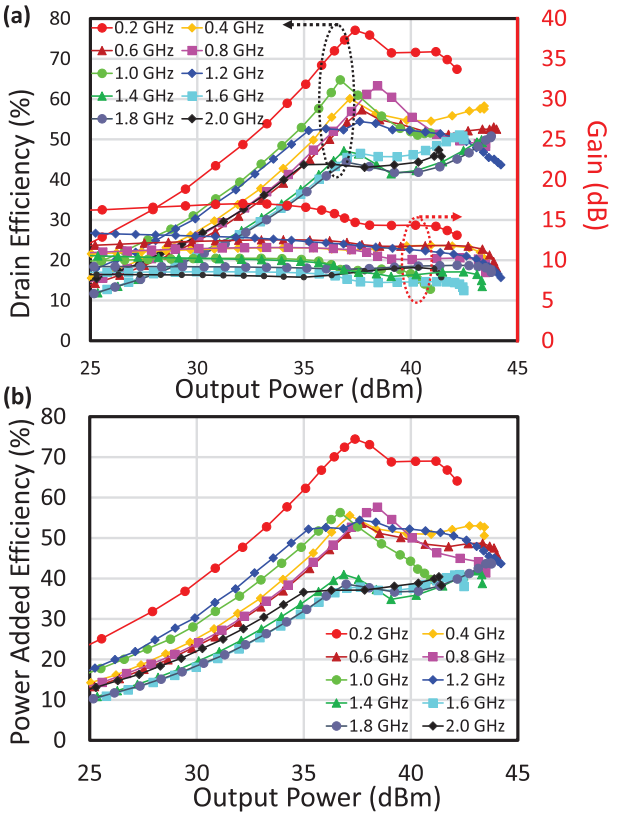

Fig. 19. (a) Power-swept measurement of drain efficiency and gain from 0.2 to 2 GHz. (b) Measured power added efficiency.

OBO levels. The corresponding measured peak efficiency falls within the range of 44%–67%, and the efficiencies at 6 dB OBOs are in the range of 43%–75%. The power-dependent gain and efficiency profiles at various frequencies are shown in Fig. 19, which indicates a strong efficiency enhancement across different power levels.

Table II presents a comparison between this design and other recently published load-modulated PAs. Notably, the proposed DL-LMBA demonstrates a decade bandwidth, the highest bandwidth among all reported DL-LMBAs, while

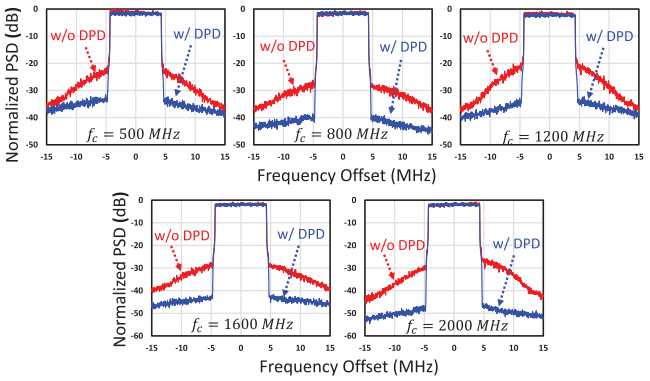

Fig. 20. Output spectrum with DPD.

maintaining a highly competitive performance in terms of drain efficiency and gain.

A detailed comparative analysis of this work with previously reported DL-LMBAs is conducted here to highlight key design trade-offs. In [22], the use of different IMNs for the BA and CA, combined with a quadrature coupler at the input, introduces significant phase dispersion, which necessitates a filter-based phase shifter and a simplified, mismatched BA OMN, ultimately compromising back-off efficiency. In contrast, [30] employs a high-impedance transformation ratio in the BA OMN and utilizes continuous-mode PA operation to enhance matching and back-off efficiency, albeit at the cost of reduced bandwidth. In this work, more linear IMN and OMN designs are implemented to reduce phase dispersion, enabling the use of a simpler transmission-line-based phase shifter. The BA OMN here has a lower impedance transformation ratio than in [30], which requires a reduced VDD to achieve the desired optimum impedance, resulting in lower peak output power. Combined with ultrawideband balun and quadrature couplers, the proposed design achieves the widest bandwidth and improved back-off efficiency compared to [22] (though over a lower frequency range), with some trade-off in peak power and efficiency relative to [30].

B. Modulated Measurements

A 10-MHz-bandwidth 5G new radio (NR) signal with a PAPR of 9.5 dB is used to perform modulated measurements. The modulated signals are generated and analyzed using Keysight PXIe vector transceiver (VXT M9421). The average power of the modulated signals is around 31–33 dBm, and the output spectrum is shown in Fig. 20 at 500, 800, 1200, 1600, and 2000 MHz, with average efficiency of 48%, 43%, 49%, 32%, and 33%, respectively. The measured adjacent channel leakage ratios (ACLR) at these frequencies are below −24 dBc. After applying DPD, the measured ACLR improves from −29.1 to −39.7 dBc at 0.8 GHz and from −30.65 to −47.1 dBc at 2.0 GHz. The corresponding measured AM–AM and AM–PM results at 2.0 GHz are shown in Fig. 21, confirming that the DL-LMBA is linearizable. Compared to our previously reported PD-LMBA prototype [48], the DL-LMBA prototype exhibits a reduced OBO range (6- versus 10-dB), but demonstrates superior performance in both linearity and linearizability. For instance, at 2.0 GHz, the measured ACLR

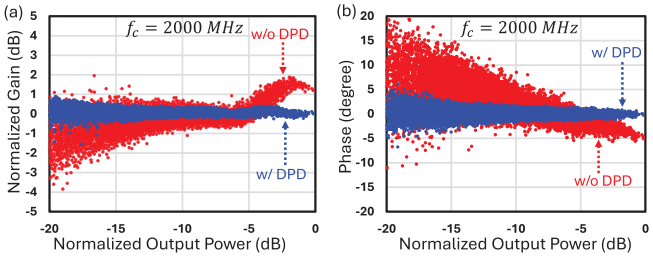

Fig. 21. Measured (a) AM–AM and (b) AM–PM with DPD.

of the PD-LMBA is −21.2/−34.1 dBc before/after DPD, which is noticeably worse than the −30.65/−47.1 dBc achieved in this work. It is worth noting that both prototypes utilize the same modulated signal and DPD algorithm, ensuring a fair comparison.

VI. Conclusion

This article demonstrates that the bandwidth of an LMBA is fundamentally constrained by the choice of power divider. For the first time, it is proven that ideal broadband load modulation behavior in a DL-LMBA can only be achieved when a constant 180° phase offset is maintained between the BA and CA signal paths across the entire frequency band. This requirement necessitates that the input power divider maintain the desired phase offset across the bandwidth. Notably, this condition contrasts with that of PD-LMBA, which requires a constant 0° phase offset. To fulfill the specific phase-alignment requirement of DL-LMBA, a novel RPB is proposed using a signal-flow-based approach. The RPB also shows potential for other applications due to its superior broadband performance. Based on the proposed theory, a decade-bandwidth DL-LMBA prototype is developed, significantly outperforming the state of the art.

Acknowledgment

The authors would like to thank Prof. Patrick Roblin of The Ohio State University for his insightful signal-flow graph of the BA from his lecture slides, and the signal-flow graph introduced in this article uses a similar drawing style. They are also thankful to Barry L. Johnson of Keysight Technologies for the technical support on DPD setup.

References

[1] J. Kim et al., "Highly efficient RF transmitter over broad average power range using multilevel envelope-tracking power amplifier," *IEEE Trans. Circuits Syst. I, Reg. Papers*, vol. 62, no. 6, pp. 1648–1657, Jun. 2015.

[2] C. M. Andersson, D. Gustafsson, J. Chani Cahuana, R. Hellberg, and C. Fager, "A 1–3-GHz digitally controlled dual-RF input power-amplifier design based on a Doherty-outphasing continuum analysis," *IEEE Trans. Microw. Theory Techn.*, vol. 61, no. 10, pp. 3743–3752, Oct. 2013.

[3] T. Barton, "Not just a phase: Outphasing power amplifiers," *IEEE Microw. Mag.*, vol. 17, no. 2, pp. 18–31, Feb. 2016.

[4] Y. Zheng and P. Roblin, "Bandwidth-enhanced mixed-mode outphasing power amplifiers based on the analytic role-exchange Doherty-Chireix continuum theory," *IEEE Trans. Circuits Syst. I, Reg. Papers*, vol. 71, no. 8, pp. 3584–3596, Aug. 2024.

[5] D. Mikrut, P. Roblin, C. Liang, S. Smith, and R. Tantawy, "Broadband outphasing power amplifier using Doherty-Chireix continuum in a GaN MMIC process," in *Proc. IEEE Topical Conf. RF/Microw. Power Model. Radio Wireless Appl.*, Jan. 2023, pp. 13–15.

[6] W. H. Doherty, "A new high efficiency power amplifier for modulated waves," *Proc. IRE*, vol. 24, no. 9, pp. 1163–1182, Sep. 1936.

[7] G. Nikandish, R. B. Staszewski, and A. Zhu, "Breaking the bandwidth limit: A review of broadband Doherty power amplifier design for 5G," *IEEE Microw. Mag.*, vol. 21, no. 4, pp. 57–75, Apr. 2020.

[8] M. Özen, K. Andersson, and C. Fager, "Symmetrical Doherty power amplifier with extended efficiency range," *IEEE Trans. Microw. Theory Techn.*, vol. 64, no. 4, pp. 1273–1284, Apr. 2016.

[9] J. J. Moreno Rubio, V. Camarchia, M. Pirola, and R. Quaglia, "Design of an 87% fractional bandwidth Doherty power amplifier supported by a simplified bandwidth estimation method," *IEEE Trans. Microw. Theory Techn.*, vol. 66, no. 3, pp. 1319–1327, Mar. 2018.

[10] Y. Xu, J. Pang, X. Wang, and A. Zhu, "Enhancing bandwidth and back-off range of Doherty power amplifier with modified load modulation network," *IEEE Trans. Microw. Theory Techn.*, vol. 69, no. 4, pp. 2291–2303, Apr. 2021.

[11] H. Lyu and K. Chen, "Analysis and design of reconfigurable multiband mismatch-resilient quasi-balanced Doherty power amplifier for massive MIMO systems," *IEEE Trans. Microw. Theory Techn.*, vol. 70, no. 10, pp. 4410–4421, Oct. 2022.

[12] H. Lyu, Y. Cao, and K. Chen, "Linearity-enhanced quasi-balanced Doherty power amplifier with mismatch resilience through series/parallel reconfiguration for massive MIMO," *IEEE Trans. Microw. Theory Techn.*, vol. 69, no. 4, pp. 2319–2335, Apr. 2021.

[13] X. Zhang, S. Li, and T. Chi, "A millimeter-wave watt-level Doherty power amplifier in silicon," *IEEE Trans. Microw. Theory Techn.*, vol. 72, no. 3, pp. 1674–1686, Mar. 2024.

[14] C. Liang, P. Roblin, Y. Hahn, J. I. Martinez-Lopez, H.-C. Chang, and V. Chen, "Single-input broadband hybrid Doherty power amplifiers design relying on a phase sliding-mode of the load modulation scheme," *IEEE Trans. Microw. Theory Techn.*, vol. 71, no. 4, pp. 1550–1562, Apr. 2023.

[15] X. Fang, J. Shi, C. Wei, Y. Duan, P. Li, and Z. Wang, "A linear millimeter-wave GaN MMIC Doherty power amplifier with improved AM-AM and AM-PM characteristics," *IEEE Trans. Microw. Theory Techn.*, vol. 72, no. 8, pp. 1–14, Aug. 2024.

[16] X.-H. Fang, H.-Y. Liu, K.-K.-M. Cheng, and S. Boumaiza, "Modified Doherty amplifier with extended bandwidth and back-off power range using optimized peak combining current ratio," *IEEE Trans. Microw. Theory Techn.*, vol. 66, no. 12, pp. 5347–5357, Dec. 2018.

[17] J. Xia, W. Chen, F. Meng, C. Yu, and X. Zhu, "Improved three-stage Doherty amplifier design with impedance compensation in load combiner for broadband applications," *IEEE Trans. Microw. Theory Techn.*, vol. 67, no. 2, pp. 778–786, Feb. 2019.

[18] E. Liu and H. Wang, "A broadband four-way parallel–series Doherty power amplifier for 5G communications," *IEEE J. Solid-State Circuits*, vol. 59, no. 5, pp. 1312–1322, May 2024.

[19] D. J. Shepphard, J. Powell, and S. C. Cripps, "An efficient broadband reconfigurable power amplifier using active load modulation," *IEEE Microw. Wireless Compon. Lett.*, vol. 26, no. 6, pp. 443–445, Jun. 2016.

[20] D. J. Shepphard, J. Powell, and S. C. Cripps, "A broadband reconfigurable load modulated balanced amplifier (LMBA)," in *IEEE MTT-S Int. Microw. Symp. Dig.*, Jun. 2017, pp. 947–949.

[21] R. Quaglia and S. Cripps, "A load modulated balanced amplifier for telecom applications," *IEEE Trans. Microw. Theory Techn.*, vol. 66, no. 3, pp. 1328–1338, Mar. 2018.

[22] P. H. Pednekar, E. Berry, and T. W. Barton, "RF-input load modulated balanced amplifier with octave bandwidth," *IEEE Trans. Microw. Theory Techn.*, vol. 65, no. 12, pp. 5181–5191, Dec. 2017.

[23] P. H. Pednekar, W. Hallberg, C. Fager, and T. W. Barton, "Analysis and design of a Doherty-like RF-input load modulated balanced amplifier," *IEEE Trans. Microw. Theory Techn.*, vol. 66, no. 12, pp. 5322–5335, Dec. 2018.

[24] Y. Cao and K. Chen, "Pseudo-Doherty load-modulated balanced amplifier with wide bandwidth and extended power back-off range," *IEEE Trans. Microw. Theory Techn.*, vol. 68, no. 7, pp. 3172–3183, Jul. 2020.

[25] J. Pang et al., "Analysis and design of highly efficient wideband RF-input sequential load modulated balanced power amplifier," *IEEE Trans. Microw. Theory Techn.*, vol. 68, no. 5, pp. 1741–1753, May 2020.

[26] Y. Cao, H. Lyu, and K. Chen, "Asymmetrical load modulated balanced amplifier with continuum of modulation ratio and dual-octave bandwidth," *IEEE Trans. Microw. Theory Techn.*, vol. 69, no. 1, pp. 682–696, Jan. 2021.

[27] J. Guo, Y. Cao, and K. Chen, "1-D reconfigurable pseudo-Doherty load modulated balanced amplifier with intrinsic VSWR resilience across wide bandwidth," *IEEE Trans. Microw. Theory Techn.*, vol. 71, no. 6, pp. 2465–2478, Jun. 2023.

[28] C. Chu, J. Pang, R. Darraji, S. K. Dhar, T. Sharma, and A. Zhu, "Broadband sequential load modulated balanced amplifier with extended design space using second harmonic manipulation," *IEEE Trans. Microw. Theory Techn.*, vol. 71, no. 5, pp. 1990–2003, May 2023.

[29] C. Belchior, L. C. Nunes, P. M. Cabral, and J. C. Pedro, "Sequential LMBA design technique for improved bandwidth considering the balanced amplifiers off-state impedance," *IEEE Trans. Microw. Theory Techn.*, vol. 71, no. 8, pp. 3629–3643, Aug. 2023.

[30] J. Pang, C. Chu, Y. Li, and A. Zhu, "Broadband RF-input continuous-mode load-modulated balanced power amplifier with input phase adjustment," *IEEE Trans. Microw. Theory Techn.*, vol. 68, no. 10, pp. 4466–4478, Oct. 2020.

[31] J. Xie, K.-K.-M. Cheng, P. Yu, and X. Fang, "Dual-band pseudo-Doherty load modulated balanced amplifier design with arbitrarily selected frequency bands," *IEEE Trans. Circuits Syst. II, Exp. Briefs*, vol. 71, no. 8, pp. 3665–3669, Aug. 2024.

[32] J. Xie, K.-K. M. Cheng, X. Fang, and P. Yu, "Extension of output backoff range in three-stage load modulated balanced amplifier using asymmetric coupling and non{-} z_0 load," *IEEE Trans. Microw. Theory Techn.*, vol. 73, no. 1, pp. 553–567, Jan. 2024.

[33] N. B. Vangipurapu, P. Gong, J. Guo, and K. Chen, "Indirectly-non-reciprocal load modulated balanced amplifier with equivalent operation at antenna interface," in *IEEE MTT-S Int. Microw. Symp. Dig.*, Jun. 2024, pp. 1032–1035.

[34] Y. Cao, S. P. Gowri, N. B. Vangipurapu, and K. Chen, "High-power BAW-based FDD front-end using indirect-duplexing load modulated balanced amplifier for massive MIMO array," in *IEEE MTT-S Int. Microw. Symp. Dig.*, Jun. 2024, pp. 485–488.

[35] N. B. Vangipurapu, H. Lyu, Y. Cao, and K. Chen, "Intrinsically mode-reconfigurable load-modulation power amplifier leveraging transistor's analog-digital duality," in *IEEE MTT-S Int. Microw. Symp. Dig.*, Jun. 2022, pp. 418–421.

[36] J. Guo and K. Chen, "Reconfigurable hybrid asymmetrical load modulated balanced amplifier with high linearity, wide bandwidth, and load insensitivity," in *IEEE MTT-S Int. Microw. Symp. Dig.*, Jun. 2023, pp. 462–465.

[37] H. Jia, R. Liu, Q. Wu, and A. Zhu, "A 26-GHz GaN MMIC load-modulated balanced amplifier with miniaturized dual-loop coupler," *IEEE Trans. Microw. Theory Techn.*, vol. 73, no. 1, pp. 530–539, Jan. 2025.

[38] J. Guo, Y. Cao, and K. Chen, "Linear hybrid asymmetrical load-modulated balanced amplifier with multiband reconfigurability and antenna-vswr resilience," *IEEE Trans. Microw. Theory Techn.*, vol. 72, no. 9, pp. 5319–5332, Sep. 2024.

[39] S. F. B. Faruquee, J. Guo, P. Gong, and K. Chen, "Hybrid load-modulated double-balanced amplifier (H-LMDBA) with four-way load modulation and >15-dB power back-off range," in *Proc. IEEE Wireless Microw. Technol. Conf. (WAMICON)*, Apr. 2024, pp. 1–4.

[40] C. Chu et al., "Waveform engineered sequential load modulated balanced amplifier with continuous class-F-1 and Class-J operation," *IEEE Trans. Microw. Theory Techn.*, vol. 70, no. 2, pp. 1269–1283, Feb. 2022.

[41] P. Chen et al., "A theoretical method to optimize the control signal power for high-efficiency symmetrical load modulated balanced amplifier designs," *IEEE Microw. Wireless Technol. Lett.*, vol. 34, no. 2, pp. 211–214, Feb. 2024.

[42] J. Guo, P. Gong, and K. Chen, "Theory and design of pseudo-Doherty load-modulated double balanced amplifier with intrinsic insensitivity to antenna VSWR," *IEEE Trans. Circuits Syst. I, Reg. Papers*, vol. 72, no. 5, pp. 2048–2060, May 2025.

[43] H. Zhou, J.-R. Pérez-Cisneros, B. Langborn, T. Eriksson, and C. Fager, "A wideband and highly efficient circulator load modulated power amplifier architecture," *IEEE Trans. Circuits Syst. I, Reg. Papers*, vol. 70, no. 8, pp. 3117–3129, Aug. 2023.

[44] X. Chen, M. Zhao, W. Chen, and Z. Feng, "A 700–2800MHz switchless class-G power amplifier with two-quadrant modulation for back-off efficiency improvement," in *IEEE MTT-S Int. Microw. Symp. Dig.*, Jun. 2022, pp. 410–413.

[45] X. Fang, R. Chen, and J. Shi, "Switchless Class-G power amplifiers: Generic theory and design methodology using packaged transistors," *IEEE Trans. Microw. Theory Techn.*, vol. 72, no. 8, pp. 4625–4637, Aug. 2024.

[46] L. V. Guansheng, W. Chen, X. Chen, F. Huang, and Z. Feng, "5.1 a GaN SLCG-Doherty-continuum power amplifier achieving >38% 6dB back-off efficiency over 1.35 to 7.6GHz," in *IEEE Int. Solid-State Circuits Conf. (ISSCC) Dig. Tech. Papers*, Feb. 2025, pp. 1–3.

[47] T.-Y. Huang, N. S. Mannem, S. Li, D. Jung, M.-Y. Huang, and H. Wang, "A coupler balun load-modulated power amplifier with extremely wide bandwidth," *IEEE Trans. Microw. Theory Techn.*, vol. 71, no. 4, pp. 1573–1586, Apr. 2023.
[48] P. Gong, J. Guo, N. Bharadwaj Vangipurapu, and K. Chen, "Signal-flow-based analysis and design of pseudo-Doherty load-modulated balanced amplifier toward unlimited RF bandwidth," *IEEE Trans. Microw. Theory Techn.*, vol. 73, no. 1, pp. 206–220, Jan. 2025.
[49] V. Qunaj and P. Reynaert, "A Ka-band Doherty-like LMBA for high-speed wireless communication in 28-nm CMOS," *IEEE J. Solid-State Circuits*, vol. 56, no. 12, pp. 3694–3703, Dec. 2021.
[50] B. Yoon, S. Bae, S. Lee, S. Hwang, J. Jeon, and J. Kim, "A broadband Doherty-like load-modulated balanced amplifier with an optimized impedance transformation ratio in InGaP/GaAs HBT process for handset applications," *IEEE Microw. Wireless Technol. Lett.*, vol. 35, no. 6, pp. 848–851, Jun. 2025.
[51] P. Gong, N. B. Vangipurapu, J. Guo, and K. Chen, "RF-input Doherty-like load-modulated balanced amplifier with decade bandwidth enabled by novel broadband 180° power divider," *IEEE Microw. Wireless Technol. Lett.*, vol. 35, no. 6, pp. 860–863, Jun. 2025.
[52] W. Zhu et al., "32.8 a 27.8-to-38.7GHz load-modulated balanced power amplifier with scalable 7-to-1 load-modulated power-combine network achieving 27.2dBm output power and 28.8%/23.2%/16.3%/11.9% Peak/6/9/12dB back-off efficiency," in *IEEE Int. Solid-State Circuits Conf. (ISSCC) Dig. Tech. Papers*, Feb. 2024, pp. 534–536.
[53] L. Chen, H. Liu, J. Hora, J. A. Zhang, K. S. Yeo, and X. Zhu, "A monolithically integrated single-input load-modulated balanced amplifier with enhanced efficiency at power back-off," *IEEE J. Solid-State Circuits*, vol. 56, no. 5, pp. 1553–1564, May 2021.
[54] C. Tseng and Y.-C. Hsiao, "A new broadband Marchand balun using slot-coupled microstrip lines," *IEEE Microw. Wireless Compon. Lett.*, vol. 20, no. 3, pp. 157–159, Mar. 2010.
[55] F. Wang and H. Wang, "A broadband linear ultra-compact mm-wave power amplifier with distributed-balun output network: Analysis and design," *IEEE J. Solid-State Circuits*, vol. 56, no. 8, pp. 2308–2323, Aug. 2021.
[56] D. M. Pozar, *Microwave Engineering*, 3rd ed., Hoboken, NJ, USA: Wiley, 2005. [Online]. Available: https://cds.cern.ch/record/882338
[57] T.-W. Li and H. Wang, "A millimeter-wave fully integrated passive reflection-type phase shifter with transformer-based multi-resonance loads for 360° phase shifting," *IEEE Trans. Circuits Syst. I, Reg. Papers*, vol. 65, no. 4, pp. 1406–1419, Apr. 2018.
[58] R. Garg and A. S. Natarajan, "A 28-GHz low-power phased-array receiver front-end with 360° RTPS phase shift range," *IEEE Trans. Microw. Theory Techn.*, vol. 65, no. 11, pp. 4703–4714, Nov. 2017.
[59] A. Romano, T. Sonnenberg, and Z. Popović, "50–110-GHz continuous GaN MMIC reflective phase shifters," *IEEE Trans. Microw. Theory Techn.*, vol. 72, no. 3, pp. 1634–1642, Mar. 2024.
[60] K. Hagiwara and H. Arai, "Wideband unbalanced fed 180-degree phase shifter using phase inverter," in *Proc. IEEE Int. Workshop Electromagn., Appl. Student Innov. Competition*, Aug. 2013, pp. 76–77.
[61] Y. Bi, Y. Wang, and K. Ma, "A 2-to-67 GHz balun based on the SISL platform," *IEEE Trans. Microw. Theory Techn.*, vol. 73, no. 4, pp. 2195–2205, Apr. 2025.

Pingzhu Gong (Student Member, IEEE) received the B.Eng. degree in electrical engineering from Tianjin University, Tianjin, China, in 2019, and the M.S. degree in electrical and computer engineering from The Ohio State University, Columbus, OH, USA, in 2022. He is currently pursuing the Ph.D. degree in electrical engineering at the University of Central Florida, Orlando, FL, USA.

His research interests include highly efficient and broadband power amplifier (PA) architectures in CMOS and GaN technologies, as well as passive components such as couplers, phase shifters, and baluns.

Mr. Gong was a recipient of the First Place Award of the Student Design Competition on High Efficiency Power Amplifier at IEEE MTT-S IMS in 2025. His paper was selected as a Finalist (Top 10) in the Best Student Paper Competition at IEEE MTT-S International Microwave Symposium (IMS) in 2024 and 2025.

Niteesh Bharadwaj Vangipurapu (Graduate Student Member, IEEE) received the bachelor's degree in electronics and communication engineering from Visvesvaraya Technological University, Belgaum, India, in 2020, and the M.S. degree in electrical engineering from the University of Central Florida, Orlando, FL, USA, in 2022, where he is currently pursuing the Ph.D. degree.

His research interests include novel, highly efficient, and linear power amplifier (PA) architectures. He is currently working on the design of RF/mm-Wave circuits.

Mr. Vangipurapu was a recipient of the First Place Award of the High Efficiency Power Amplifier Student Design Competition (HEPA-SDC) in the IEEE MTT-S International Microwave Symposium (IMS) 2025. He was the winner of the First Place Award of Student Paper Competition in IEEE WAMICON 2023. He currently serves as the Vice Chair of the IEEE MTT-S/AP-S Orlando Chapter.

Jiachen Guo (Member, IEEE) received the M.S. degree in computer engineering from Syracuse University, Syracuse, NY, USA, in 2021. He is currently pursuing the Ph.D. degree in electrical engineering at the University of Central Florida, Orlando, FL, USA.

His research interests include novel highly efficient broadband and linear power amplifier (PA) architectures and reconfigurable RF/millimeter-wave circuit designs.

Mr. Guo was a recipient of the Second Place Award in the Student Design Competition on High-Efficiency Power Amplifiers at IEEE MTT-S IMS 2022 and the First Place Award in the same competition at IEEE MTT-S IMS 2025.

Kenle Chen (Senior Member, IEEE) received the bachelor's degree in communication engineering from Xi'an Jiaotong University, Xi'an, Shaanxi, China, in 2005, the master's degree in electronics and information engineering from Peking University, Beijing, China, in 2008, and the Ph.D. degree in electrical engineering from Purdue University, West Lafayette, IN, USA, in 2013.

He is currently an Associate Professor at the Department of Electrical and Computer Engineering, University of Central Florida, Orlando, FL, USA. His research interests include energy-efficient, wideband, and ultrahigh-speed RF/mm-wave circuits and systems for 5G-and-beyond communications, extreme-performance power amplifiers in CMOS and compound semiconductor technologies, reconfigurable RF/mm-Wave electronics, and innovational wireless radio concepts/architectures/applications. Prior to his career in academia, he has extensive experience in wireless and semiconductor industries. From 2015 to 2017, he worked as a Staff RFIC Engineer at Skyworks Solutions Inc., where he focused on development of RF frontend modules for the advanced Smart-Phone platforms. From 2013 to 2015, he worked as a Principal/Lead RFIC Engineer at innovational startups, where he led the Research and Development of multiple successful products of CMOS-integrated power amplifiers and frontend solutions for the latest WLAN platforms, e.g., IEEE802.11ac/ax.

Dr. Chen was a recipient of 2012 IEEE Microwave Theory and Techniques Society (MTT-S) graduate fellowship. He is an Associate Editor of *IEEE Transactions on Microwave Theory and Techniques*.